Science Advances
AAAS

advances.sciencemag.org/cgi/content/full/7/10/eabe8691/DC1

Supplementary Materials for

Enhanced tunable second harmonic generation from twistable interfaces and vertical superlattices in boron nitride homostructures

Kaiyuan Yao, Nathan R. Finney, Jin Zhang, Samuel L. Moore, Lede Xian, Nicolas Tancogne-Dejean, Fang Liu, Jenny Ardelean, Xinyi Xu, Dorri Halbertal, K. Watanabe, T. Taniguchi, Hector Ochoa, Ana Asenjo-Garcia, Xiaoyang Zhu, D. N. Basov, Angel Rubio, Cory R. Dean, James Hone*, P. James Schuck*

*Corresponding author. Email: jh2228@columbia.edu (J.H.); p.j.schuck@columbia.edu (P.J.S.)

Published 3 March 2021, *Sci. Adv.* **7**, eabe8691 (2021)
DOI: 10.1126/sciadv.abe8691

This PDF file includes:

Sections S1 to S9
Figs. S1 to S13
References

S1. Nonlinear transfer matrix method

A numerical model is developed to compute nonlinear frequency conversions in layered van der Waals (vdW) stacks, which allows for implementation of an arbitrary symmetry group, twist angle and nonlinear efficiency into each composite layer. Nonlocal multipole moments of the nonlinear polarization are incorporated. Phase-matching effects and multilayer reflections are included. The method is based on a transfer matrix formalism initially employed for studying generation and propagation of high harmonic electromagnetic waves in multilayer nonlinear thin films [23]. The model proposed in Ref.[23] calculates third harmonic generation. In this work it is adapted to calculate second harmonic generation (SHG) from multilayered hexagonal boron nitride (BN) rotators, with polarization resolution and arbitrary crystal orientation for each layer. Owing to the nature of transfer matrix formalism, it is also convenient to resolve the SHG contribution from each single layer of BN, allowing us to separately compute the interface and bulk effects. Each BN layer within the rotator structure is modeled by linear refractive indexes of bulk BN in the visible and near infrared region [45], and the thickness is assumed to be the interlayer spacing, i.e. 0.334 nm. Interlayer couplings are not included, and each layer is assumed to be a rigid plate without any lattice reconstruction or strain effects. The depletion of the pump field due to frequency conversion is also neglected, which is a good approximation for relatively low field experiments. This model may be also applied for calculating other complex vdW heterostructures in the frequency range where interlayer coupling is minimal.

The principle of the nonlinear transfer matrix calculation is illustrated by Fig. S1 and summarized as follows. In this coordinate system, $+z$ is the out-of-plane direction pointing from air to substrate. Each layer is indexed by numbers 0, 1, ... i, j, k, ... $f-1$, f, with 0 being air, f being the substrate, and 1, 2, .. $f-1$ representing monolayer BN. The crystal orientation of each BN layer is described by φ^j which is the angle between BN armchair direction and the $+y$ direction, as shown by Fig. S1. The pump field in any layer j is described as a two-component pseudovector $\boldsymbol{E}^j_{\omega,y} = [E^{j,+}_{\omega,y}, E^{j,-}_{\omega,y}]$ where $E^{j,+}_{\omega,y}$ ($E^{j,-}_{\omega,y}$) is the complex amplitude of forward (backward) propagating electric field. Without loss of generality the incident pump field is set to be along the $+y$ direction in the lab frame. Since the linear index of BN is in-plane isotropic, the polarization of the pump field in each layer will be preserved and will be along the y direction (but with different phases). For polarization dependent calculations, we rotate crystallographic orientation of the BN layers by setting arbitrary φ^j for each layer, which is equivalent to a rotation of optical polarization. Fig. S1a illustrates the calculation of SHG contribution from layer j. In low pump field regime, depletion of the pump field can be neglected [23], thus the nonlinear electric field contribution from each layer can be linearly summed together to obtain the total response. In the source layer j with nonzero $\chi^{(2)}$, the nonlinear polarization $\boldsymbol{P}^j_{2\omega,y}$ and $\boldsymbol{P}^j_{2\omega,x}$ generate bound waves at frequency 2ω, which are represented by $\boldsymbol{E}^j_{S,y} = [E^{j,+}_{S,y}, E^{j,-}_{S,y}]$ and $\boldsymbol{E}^j_{S,x} = [E^{j,+}_{S,x}, E^{j,-}_{S,x}]$. Then the bound waves in the source layer drives free waves at 2ω frequency (denoted $\boldsymbol{E}^j_{2\omega,y}$and $\boldsymbol{E}^j_{2\omega,x}$) in all the layers, including the reflected SHG wave collected experimentally in the air medium.

The detailed calculation steps are described below. The wave propagation of the pump field and the SHG field through the multilayer structure are calculated following standard linear optical transfer matrix methods used in previous work [25]. The field pseudovectors in neighboring layers are related by transfer matrices $\boldsymbol{M}^{ij}$ which are calculated for the proper frequency (ω or 2ω) and polarization (x or y) based on the Fresnel reflection and transmission coefficients r^{ij} and t^{ij}. The total transfer matrix $\boldsymbol{T}$ for the specific frequency (ω or 2ω) and polarization (x or y) can then be calculated as follows:

$$\boldsymbol{E}^i = \boldsymbol{M}^{ij}\boldsymbol{E}^i \tag{S1}$$

$$\boldsymbol{M}^{ij} = \frac{1}{t^{ij}}\begin{bmatrix} 1 & r^{ij} \\ r^{ij} & 1 \end{bmatrix} \tag{S2}$$

$$\boldsymbol{T} = \boldsymbol{M}^{f(f-1)}\boldsymbol{\Phi}^{(f-1)}\boldsymbol{M}^{(f-1)(f-2)}\boldsymbol{\Phi}^{(f-2)}...\boldsymbol{M}^{10} \tag{S3}$$

$$\boldsymbol{\Phi}^i = \begin{bmatrix} \phi^i & 0 \\ 0 & \frac{1}{\phi^i} \end{bmatrix} \tag{S4}$$

where $\phi^i = e^{in_\omega k^0_\omega d^i}$, wherein $k^0_\omega = \omega/c$ (or $2\omega/c$) satisfies $(k_{\omega,x})^2 + (k^i_{\omega,z})^2 = \epsilon_i(k^0_\omega)^2$ for a free wave propagating in layer i with wavevector $\vec{\boldsymbol{k}}^i_\omega = [k_{\omega,x}, k_{\omega,y}, k^i_{\omega,z}]^T$ (note, c is the speed of light), $n^i_\omega = n^i(\omega) + i\kappa^i(\omega)$ where $n^i(\omega)$ and $\kappa^i(\omega)$ are the frequency-dependent real and imaginary components of the linear refractive index n_ω in layer i respectively, and d^i is equal to the thickness of layer i (0.334 nm for the BN layers, ∞ for the air above and substrate below the stack).

Within BN layer j, the elementary nonlinear polarization is $P^j_{2\omega,\alpha}$ where α denotes the polarization direction (α = x or y). In general, $P^j_{2\omega,\alpha}$ includes multipole contributions, with the dipole moment $P^{j,d}_{2\omega,\alpha}$, quadrupole moment $P^{j,q}_{2\omega,\alpha}$, and higher order terms with decreasing magnitudes in the low-field regime:

$$\begin{aligned} P^j_{2\omega,\alpha} &= P^{j,d}_{2\omega,\alpha} + P^{j,q}_{2\omega,\alpha} + ... \\ &= \epsilon_0\chi^{(2)}_{\alpha\beta\gamma}E^j_{\omega,\beta}E^j_{\omega,\gamma} + \epsilon_0\chi^{q,1L}_{\alpha\beta\gamma z}E^j_{\omega,\beta}\frac{\partial E^j_{\omega,\gamma}}{\partial z} + ... \end{aligned} \tag{S5}$$

Here $\chi^{(2)}_{\alpha\beta\gamma}$ are elements of the nonlinear susceptibility tensor $\boldsymbol{\chi}^{(2)}$ with the subscripts α, β, γ denoting in-plane polarization directions in Cartesian coordinates. $\chi^{q,1L}_{\alpha\beta\gamma z}$ are elements of quadrupolar nonlinear susceptibility tensor $\boldsymbol{\chi}^{q,1L}$ for the quadrupole moment from a monolayer BN. The last subscript is fixed to be z as only plane waves are considered in the calculation. ϵ_0 is the vacuum permittivity. $E^j_{\omega,\beta}$ is the complex amplitude of the pump electric field in layer j polarized along the β direction. Note that we follow the Einstein notation for summing over subscripts α, β, γ whenever they are repeated.

Since each monolayer BN belongs to the point group of D_{3h}, its nonvanishing $\boldsymbol{\chi}^{(2)}$ tensor elements are:

$$\chi^{(2)}_{y'y'y'} = -\chi^{(2)}_{y'x'x'} = -\chi^{(2)}_{x'x'y'} = -\chi^{(2)}_{x'y'x'} = |\chi^{(2)}| \tag{S6}$$

with x' and y' being the zigzag and armchair orientations as shown by Fig. S1. We note that in this section we use primed (') coordinates for the material frame–elsewhere we drop the prime when it is implicit that subscripts refer to the material frame.

The monolayer quadrupole moments $P^{j,q}_{2\omega,\alpha}$ in (S5) will vanish due to the reflection symmetry σ_h in the D_{3h} point group, i.e., $\chi^{q,1L}_{\alpha\beta\gamma z} = 0$. In the case of normal incidence, the minimum unit structure to hold a quadrupole moment is a bilayer BN that breaks σ_h. In our transfer matrix computational method, the bilayer quadrupole moment arises from the variation of elementary dipole moments across neighbouring monolayers as a result of the gradient of the pump electric field. For example, consider nonlinear polarization from an AA'-stacked bilayer unit including layer j and $j+1$ is, where the dipole moment vanishes due to centrosymmetry leaving the quadrupole moment as the leading term:

$$\begin{aligned} P^{j,j+1,q}_{2\omega,\alpha} &= P^{j,d}_{2\omega,\alpha} + P^{j+1,d}_{2\omega,\alpha} \\ &= \epsilon_0\chi^{(2)}_{\alpha\beta\gamma}(E^{j+1}_{\omega,\beta}E^{j+1}_{\omega,\gamma} - E^j_{\omega,\beta}E^j_{\omega,\gamma}) \\ &= 2\epsilon_0\chi^{(2)}_{\alpha\beta\gamma}d_{BN}E^j_{\omega,\beta}\frac{\partial E^j_{\omega,\gamma}}{\partial z} + ... \end{aligned} \tag{S7}$$

with d_{BN} representing the BN interlayer distance. From (S7), we note that our transfer matrix model is equivalent to taking the quadrupole susceptibility $\chi^{q,2L}_{\alpha\beta\gamma z}$ for an AA'-stacked bilayer unit as:

$$\chi^{q,2L}_{\alpha\beta\gamma z} = 2\chi^{(2)}_{\alpha\beta\gamma}d_{BN} \tag{S8}$$

This is consistent with the expectation that relative contribution of increasingly higher-order multipole moments scale like ak, where a is the typical atomic dimension of the system, and k is the typical magnitude of wave vector [2].

Next the model computes how the nonlinear polarizations drive second harmonic waves and their propagation throughout the structure. Due to multilayer reflections, the electric field $E^j_{\omega,\beta}$ is a superposition of both forward and backward propagating waves:

$$E^j_{\omega,\beta} = E^{j,+}_{\omega,\beta}e^{ik_\omega z} + E^{j,-}_{\omega,\beta}e^{-ik_\omega z} \tag{S9}$$

Here $k_\omega = n_\omega k^0_\omega$ is the reduced wavevector, k^0_ω is free-space wavevector, and n_ω is the linear refractive index all evaluated at the pump frequency ω.

Without loss of generality, the pump polarization is fixed along the y direction, and the twist angle of each layer is φ^j for layer j as shown in Fig. S1. Therefore, the nonlinear polarization in layer j can be expressed as:

$$P^j_{2\omega,y} = \epsilon_0|\chi^{(2)}|cos(3\varphi^j)\left[E^{j,+}_{\omega,y}e^{ik_\omega z} + E^{j,-}_{\omega,y}e^{-ik_\omega z}\right]^2 \tag{S10}$$

$$P^{j}_{2\omega,x} = \epsilon_0 |\chi^{(2)}| sin(3\varphi^j) \left[E^{j,+}_{\omega,x} e^{ik_\omega z} + E^{j,-}_{\omega,x} e^{-ik_\omega z}\right]^2 \tag{S11}$$

As a result of mixing forward- and backward-propagating waves in Eq. (S10) and Eq. (S11), nonlinear polarizations with different wavevectors ($\pm 2k_\omega$ or ± 0) will be generated. Although the phase change within the source layer j is negligible due to the atomic thickness of monolayer BN, the different wavevectors will lead to appreciably different propagation effects when the whole device structure with hundreds of layers is considered. Therefore the nonlinear polarization pseudovector $\boldsymbol{P}$ has four contributions accounting for different polarization directions (x or y) and different wavevectors ($\pm 2k_\omega$ or ± 0). These are written in the pseudovector form as below:

$$\boldsymbol{P}^{j,2k_\omega}_{2\omega,y} = \epsilon_0 |\chi^{(2)}| cos(3\varphi^j) \begin{bmatrix} {E^{j,+}_{\omega,y}}^2 \\ {E^{j,-}_{\omega,y}}^2 \end{bmatrix} \tag{S12}$$

$$\boldsymbol{P}^{j,2k_\omega}_{2\omega,x} = \epsilon_0 |\chi^{(2)}| sin(3\varphi^j) \begin{bmatrix} {E^{j,+}_{\omega,y}}^2 \\ {E^{j,-}_{\omega,y}}^2 \end{bmatrix} \tag{S13}$$

$$\boldsymbol{P}^{j,0}_{2\omega,y} = \epsilon_0 |\chi^{(2)}| cos(3\varphi^j) \begin{bmatrix} E^{j,+}_{\omega,y} E^{j,-}_{\omega,y} \\ E^{j,+}_{\omega,y} E^{j,-}_{\omega,y} \end{bmatrix} \tag{S14}$$

$$\boldsymbol{P}^{j,0}_{2\omega,x} = \epsilon_0 |\chi^{(2)}| sin(3\varphi^j) \begin{bmatrix} E^{j,+}_{\omega,y} E^{j,-}_{\omega,y} \\ E^{j,+}_{\omega,y} E^{j,-}_{\omega,y} \end{bmatrix} \tag{S15}$$

The nonlinear polarization terms above serve as the sources in generating second harmonic waves. In the low-field regime, depletion of the pump beam can be neglected, and we can solve decoupled inhomogeneous wave equations for 2ω [1]. As shown by (S12)-(S15), there are in total eight independent nonlinear polarization sources (for two polarizations x and y, two wavevectors $2k_\omega$ and 0, and forward/backward propagating directions). For the y-polarized forward-propagating polarization with a wave vector of $2k_\omega$, the inhomogeneous wave equation in layer j is:

$$\frac{\partial^2 E^{j}_{2\omega,y}}{\partial z^2} + k^2_{2\omega} E_{2\omega,y} = -\frac{4\pi(2\omega)^2}{c^2} P^{j,2k_\omega,+}_{2\omega,y} \tag{S16}$$

with $k_{2\omega}$ being the reduced wavevector $k_{2\omega} = n(2\omega)2\omega/c$. The solution to (S16) is

$$\begin{aligned} E^{j,2k_\omega,+}_{2\omega,y} &= E^{j,+}_{2\omega,y} e^{ik_{2\omega} z} + E^{j,2k_\omega,+}_{S,y} e^{i2k_\omega z} \\ &= E^{j,+}_{2\omega,y} e^{ik_{2\omega} z} + \frac{4\pi}{\epsilon_\omega - \epsilon_{2\omega}} P^{j,2k_\omega.+}_{2\omega,y} e^{i2k_\omega z} \end{aligned} \tag{S17}$$

Here $E^{j,+}_{2\omega,y}$ is the complex amplitude of the homogeneous solution which needs to be further determined by matching boundary conditions in the transfer matrix formalism, and $E^{j,2k_\omega,+}_{S,y}$ (bound electric field) is the particular solution as determined by the source term. We note that the denominator of the bound electric field explicitly reflects a phase-matching condition, and the divergence is caused by non-depletion assumption of the pump field. Solutions for other polarizations, wavevectors, and propagation directions can be similarly obtained. The resulting particular solutions of bound electric field can be grouped into pseudovector form as:

$$\boldsymbol{E}^{j,2k_\omega}_{S,y} = \frac{4\pi}{\epsilon_\omega - \epsilon_{2\omega}} \boldsymbol{P}^{j,2k_\omega}_{2\omega,y} \tag{S18}$$

$$\boldsymbol{E}^{j,2k_\omega}_{S,x} = \frac{4\pi}{\epsilon_\omega - \epsilon_{2\omega}} \boldsymbol{P}^{j,2k_\omega}_{2\omega,x} \tag{S19}$$

$$\boldsymbol{E}^{j,0}_{S,y} = -\frac{4\pi}{\epsilon_{2\omega}} \boldsymbol{P}^{j,0}_{2\omega,y} \tag{S20}$$

$$\boldsymbol{E}^{j,0}_{S,x} = -\frac{4\pi}{\epsilon_{2\omega}} \boldsymbol{P}^{j,0}_{2\omega,x} \tag{S21}$$

The bound waves in layer j drives 2ω free waves in adjacent layers ($\boldsymbol{E}^{i,\pm}_{2\omega,y}$, $\boldsymbol{E}^{i,\pm}_{2\omega,x}$ in layer i, and similarly denoted for layer k). The free waves, being solutions to homogeneous wave equations in each layer, have wavevectors of $k_{2\omega} = n_{2\omega} k^0_{2\omega}$. The relationship between the amplitudes of the bound waves in layer j and free waves in the same layer and adjacent layers are determined by matching boundary conditions for the proper type of polarization at 2ω. The second harmonic free waves can be solved by using transfer matrix method at 2ω [23]. The y-polarization components can be derived as below, while the x-polarization expressions are similar and omitted.

$$\boldsymbol{E}^{k}_{2\omega,y} = \boldsymbol{M}^{kj}_{2\omega} \boldsymbol{\Phi}^{j}_{2\omega} (\boldsymbol{M}^{ji}_{2\omega} \boldsymbol{E}^{i}_{2\omega,y} + \boldsymbol{S}^{j,2k_\omega}_{2\omega,y} + \boldsymbol{S}^{j,0}_{2\omega,y}) \tag{S22}$$

$$\boldsymbol{S}^{j,2k_\omega}_{2\omega,y} = (\overline{\boldsymbol{\Phi}^{j}_{2\omega}} \boldsymbol{M}^{js,2k_\omega}_{2\omega} \boldsymbol{\Phi}^{2k_\omega}_{2\omega} - \boldsymbol{M}^{js,2k_\omega}_{2\omega}) \boldsymbol{E}^{j,2k_\omega}_{S,y} \tag{S23}$$

$$\boldsymbol{S}^{j,0}_{2\omega,y} = (\overline{\boldsymbol{\Phi}^{j}_{2\omega}} \boldsymbol{M}^{js,0}_{2\omega} \boldsymbol{\Phi}^{0}_{2\omega} - \boldsymbol{M}^{js,0}_{2\omega}) \boldsymbol{E}^{j,0}_{S,y} \tag{S24}$$

(Note: in the above we do not follow Einstein notation rules, i.e. we do not sum over repeated layer number indices j and S)

In the equations Eqs. (S22)-(S24), the bound waves in layer j are reformed into the effective source vectors $\boldsymbol{S}^{j,2k_\omega}_{2\omega,y}$ and $\boldsymbol{S}^{j,0}_{2\omega,y}$ for convenience. Note that in the above, $\overline{\boldsymbol{\Phi}} \equiv \boldsymbol{\Phi}^{-1}$, the matrices $\boldsymbol{M}^{kj}_{2\omega}$ and $\boldsymbol{\Phi}^{j}_{2\omega}$ are ordinary transfer matrices defined for the 2ω frequency free waves, while $\boldsymbol{M}^{js,2k_\omega}_{2\omega}$ and $\boldsymbol{\Phi}^{2k_\omega}_{2\omega}$ are pseudo transfer matrices where Fresnel reflection and transmission coefficients for the second medium (source medium s) need to be evaluated using effective indexes $n_S^{j,2k_\omega}$ and $n_S^{j,0}$ corresponding to the bound wave wavevectors $2k_\omega$ and 0:

$$n_S^{j,2k_\omega} = n_\omega^j \tag{S25}$$

$$n_S^{j,0} = 0 \tag{S26}$$

The 2ω free waves in layer i and k as obtained by Eq. (S22) can be further propagated through the entire twisted multilayer structure, giving rise to the field of transmitted and reflected SHG: $E^{f,+}_{2\omega,y}(j)$ and $E^{0,-}_{2\omega,y}(j)$. This is obtained by solving linear transfer matrix problem for the multilayer structure at frequency 2ω. These are expressed in Eqs.(S27)-(S29) below. Here the index j in the parenthesis denotes that the these output SHG fields are the contribution from nonlinear polarization generated in layer j.

$$\boldsymbol{R}^{jf}_{2\omega}\begin{bmatrix} E^{f,+}_{2\omega,y} \\ 0 \end{bmatrix} - \boldsymbol{L}^{j0}_{2\omega}\begin{bmatrix} 0 \\ E^{0,-}_{2\omega,y} \end{bmatrix} = (\boldsymbol{S}^{j,2k_\omega}_{2\omega,y} + \boldsymbol{S}^{j,0}_{2\omega,y}) \tag{S27}$$

$$\boldsymbol{R}^{jf}_{2\omega} = \overline{\boldsymbol{\Phi}^{j}_{2\omega}}\boldsymbol{M}^{jk}_{2\omega}\overline{\boldsymbol{\Phi}^{k}_{2\omega}}\boldsymbol{M}^{k(k+1)}_{2\omega}...\overline{\boldsymbol{\Phi}^{f-1}_{2\omega}}\boldsymbol{M}^{(f-1)f}_{2\omega} \tag{S28}$$

$$\boldsymbol{L}^{j0}_{2\omega} = \boldsymbol{M}^{ji}_{2\omega}\boldsymbol{\Phi}^{i}_{2\omega}\boldsymbol{M}^{i(i-1)}_{2\omega}...\boldsymbol{\Phi}^{2}_{2\omega}\boldsymbol{M}^{21}_{2\omega} \tag{S29}$$

(Note: in the above we do not follow Einstein notation rules, i.e. we do not sum over repeated layer number indices j and S)

Finally, the reflected SHG field amplitude contributed by each layer are linearly summed up to give the total SHG field polarized along the y direction ($E^{0,-}_{2\omega,y}$) and the x direction ($E^{0,-}_{2\omega,x}$). The corresponding total SHG intensities along y and x directions ($I^{tot}_{SHG,y}$ and $I^{tot}_{SHG,x}$) are computed as squared norm of the coherently summed electric fields:

$$I^{tot}_{SHG,\parallel} = I^{tot}_{SHG,y} = |E^{0,-}_{2\omega,y}|^2 = |\sum_{j=0}^{f} E^{0,-}_{2\omega,y}(j)|^2 \tag{S30}$$

$$I^{tot}_{SHG,\perp} = I^{tot}_{SHG,x} = |E^{0,-}_{2\omega,x}|^2 = |\sum_{j=0}^{f} E^{0,-}_{2\omega,x}(j)|^2 \tag{S31}$$

$$I^{tot}_{SHG} = I^{tot}_{SHG,\parallel} + I^{tot}_{SHG,\perp} \tag{S32}$$

The contribution from the interface bilayer and the rest of bulk parts of the BN rotator device are then computed as:

$$I^{interface}_{SHG} = |\sum_{j=N_{TOP}}^{N_{TOP}+1} E^{0,-}_{2\omega,y}(j)|^2 + |\sum_{j=N_{TOP}}^{N_{TOP}+1} E^{0,-}_{2\omega,x}(j)|^2 \tag{S33}$$

$$\begin{aligned} I^{bulk}_{SHG} =& |\sum_{j=0}^{N_{TOP}-1} E^{0,-}_{2\omega,y}(j) + \sum_{j=N_{TOP}+2}^{N_{TOP}+N_{BOT}+1} E^{0,-}_{2\omega,y}(j)|^2 \\ &+ |\sum_{j=0}^{N_{TOP}-1} E^{0,-}_{2\omega,x}(j) + \sum_{j=N_{TOP}+2}^{N_{TOP}+N_{BOT}+1} E^{0,-}_{2\omega,x}(j)|^2 \end{aligned} \tag{S34}$$

In this way, we numerically evaluate how interface and bulk SHG contribution varies as a function of twist angle for fabricated micro rotator devices, and compared with experimental data, as shown by Fig. S4

S2. Calculation of interfacial stacking configuration

We carried out first-principles calculations as implemented in the Vienna Ab initio Simulation Package (VASP) [42], with Perdew–Burke–Ernzerhof (PBE) exchange-correlation energy functional and projector-augmented wave (PAW) pseudopotentials [43]. We used a plane-wave cutoff of 400 eV and vacuum regions of more than 15 Å between periodically repeated slabs. The first Brillouin zone was sampled using a 10x10x1 k-point grid and vdW interactions were included using the opt88 functional [44]. All structures were fully relaxed until the force on each atom was less than 0.01 eV $\AA^{-1}$. Here, we calculated the relative energies of different stacking orders with the AB stacking order ($\Delta E = E_{shift}{-}E_{AB}$). AB stacking is the lowest-energy configuration for $\theta = 60^{circ}$ up to 14 layers as shown by calculation results in Fig. S3, and we reasonably extend that the conclusion holds for bulk BN as well.

S3. SHG enhancement factor optimization based on layer numbers

In a homostructure with N$_{TOP}$ and N$_{BOT}$ layers in the top and bottom BN crystal, the SHG intensity I$_{AA'}$ for an AA'-homostructure is dependent on N$_{TOTAL}$ and its respective parity, as shown by Fig. 1c in the main text, as well as Fig. S2c. On the other hand, the SHG intensity I$_{AB}$ for an AB-homostructure is a superposition of the interface dipolar SHG from the bilayer at the interface, and bulk SHG from the N$_{TOP}$+N$_{BOT}$-2 layers left over in the top and bottom bulk BN parts, with simulation results shown by Fig. S2b. Therefore, the SHG enhancement factor of a single device, defined here as the intensity ratio I$_{AB}$/I$_{AA'}$ between its AB-homostructure form and AA'-homostructure form can be optimized by layer number selections. The simulation results are shown by Fig. S2a. The results suggest that optimum enhancement factors can be achieved first by selecting N$_{TOTAL}$ to suppress bulk SHG in the AA' interfacial configuration, and secondly selecting N$_{BOT}$ (or equivalently, N$_{TOP}$) to enhance the dipole-allowed SHG at the AB interfacial configuration. Importantly, in the optimized devices (Devices 1 and 2), SHG from the top and bottom bulk BN are both minimized, leaving SHG predominantly coming from the interfacial bilayer, as shown by simluation in Fig. S2d-f. Finally, experimental and simulation data are compared in Fig. S2j, showing good agreement.

For micro rotator devices, the twist-angle-dependent experimental and simulation data of SHG intensities are compared in Fig. S4. For simulation results, contributions from bulk and interface can be separated. Device 1 features negligible bulk contribution. At $\theta = 60°$, as shown by the schematics on the right side of Fig. S4a, the total SHG is dominated by strong interface contribution, with a minor bulk contribution that only slightly counteracts the interface dipole moment. At $\theta = 0°$, the interface dipole moment vanishes, and the total SHG is close to zero. Similar results are observed for Device 2 which is also interface-dominated, as shown by Fig. S4b. In Device 3, as shown by the schematics on the right side of Fig. S4c, the bulk contribution from the top BN is appreciable compared to the interface contribution. This is because the N_{TOP}-1 layers in the top BN correspond to a large quadrupole SHG, as shown by Fig. 1c. At $\theta = 60°$, the aligned interface dipole moments are largely counteracted by bulk contribution from the top, resulting in only moderate SHG intensity. At $\theta = 0°$, despite vanishing interface dipole moment, the bulk contribution still persists, with intensity close to that at $\theta = 60°$. Therefore the effective tuning range of Device 3 is low. Similar results are observed for Device 4, as shown by Fig. 1d.

Comparing data listed in Fig. S2j, as well as the data shown in Fig.1c and Fig.4E of the main text, we observe a trend that the theoretical calculation and the experimental values tend to deviate with increasing total layer number. This could be originating from multiple reasons. The BN refractive index we used for the calculation may deviate from actual the experimental material, and thus the calculated optical phases of fundamental and second harmonic waves tend to be more inaccurate with longer propagation length (i.e. in thicker BN films). Additionally, potential existence of polymer residues at the interface, despite the post-annealing processes and utmost care to keep the interfacial surfaces untouched during stacking, may lead to some experimental uncertainties in both optical and AFM measurements.

S4. SHG polarization patterns of monolayer and bulk BN

Monolayer BN belongs to the D_{3h} point group [22]. The nonvanishing $\boldsymbol{\chi}^{(2)}$ elements are $\chi^{(2)}_{yyy} = -\chi^{(2)}_{yxx} = -\chi^{(2)}_{xxy} = -\chi^{(2)}_{xyx}$ where $y(x)$ refers to the armchair(zigzag) direction. In our experiments, the pump beam is linearly polarized, and the collected SHG beam with polarization parallel to the pump is selectively detected. In this colinear configuration, the measured SHG intensity $I_{SHG,\parallel}$ will be:

$$I_{SHG,\parallel} \propto |\chi^{(2)}|^2 cos^2(3\varphi) I_{pump}^2 \tag{S35}$$

where φ is the angle between monolayer BN's armchair direction and the pump polarization direction.

Bulk hexagonal BN crystal belongs to the centrosymmetric D_{3d} point group with preserved inversion symmetry, as a result of the AA' stacking between each neighbouring layers. However, when such a bulk BN film is placed on a substrate with finite refractive index, the pump field may become highly nonuniform with a large gradient along the z-direction. This is illustrated by Fig. S5c which shows the calculated z-directional profile of pump field intensity I_{pump} inside a 300-layer BN on top of a fused silica (F.S.) substrate and a 285-nm-SiO_2/Si substrate. The gradient of pump field breaks reflection symmetry along the x-y plane (*i.e.*, the plane including armchair and zigzag orientations). Therefore, dressed by the optical field, the net symmetry is reduced from D_{3d} to C_{3v} which has nonvanishing $\boldsymbol{\chi}^{(2)}$ elements of $\chi^{(2)}_{yyy} = -\chi^{(2)}_{yxx} = -\chi^{(2)}_{xxy} = -\chi^{(2)}_{xyx}$, $\chi^{(2)}_{xzx} = \chi^{(2)}_{yzy}$, $\chi^{(2)}_{xxz} = \chi^{(2)}_{yyz}$, $\chi^{(2)}_{zxx} = \chi^{(2)}_{zyy}$, and $\chi^{(2)}_{zzz}$. As a result, the same in-plane polarization dependence as in Eq. (S35) would be expected, *i.e.*, a sixfold flower pattern, where the maximum intensity is aligned with armchair orientation as shown by S5b.

S5. Locking behavior of BN rotators

In all rotatable homostructures of BN we observe locking at angles set 60° apart, meaning that at these special rotation states the BN rotators can no longer be pushed by the AFM tip. Fig. S6a illustrates the stages of a push sequence during which the locking occurs, and Fig. S6b-d shows AFM scans before and after the progression illustrated in Fig. S6a. The locking condition is found to perfectly correspond with crystallographic directions as corroborated both by alignment with straight BN edges and SHG characterization, and can therefore serve as a reference for intermediate rotation angles as measured from AFM scans.

S6. BN-Graphene-BN devices: effect of interface modification on SHG

In order to further consolidate verify the dominant role of the BN-BN interface in generating the SHG signal, monolayer graphene (G) is inserted encapsulated in between the top and bottom BN of an AB-homostructure, forming a stationery BN-G-BN device, as shown by the schematic in Fig. S7a. The graphene lattice is aligned with both top and bottom BN. Owing to its centrosymmetric crystal structure, monolayer graphene itself does not generate additional SHG under normal in-plane excitation. However, the inserted encapsulated graphene layer may substantially alter interlayer charge transfer between the interfacial bilayer BN (shaded green), and subsequently change the oscillator strength responsible for interfacial dipolar SHG. On the other hand, due to its monolayer thickness, the extra layer of graphene will only induce negligible optical phase shift to affect any bulk SHG contribution. Therefore, we can further verify the interface-dominated SHG by observing whether an inserted encapsulated monolayer graphene can cause appreciable changes in SHG intensity.

Fig. S7b shows a confocal image of a device with a BN-G-BN region, a BN-BN AB-homostructure region, as well as bare bottom and top BN regions. The emission spectra from the BN-G-BN and BN-BN regions are compared in Fig. S7c. Note that we observed a broadband of fluorescence signal from graphene, which makes the BN-G-BN appear brighter in the image in Fig. S7b. For the narrow-band SHG intensity, we found it to be significantly reduced in the BN-G-BN region as compared to BN-BN AB-homostructure region, validating our assignment of the SHG as dominated by the interfacial bilayer rather than the bulk. We note that similar results are also reported in Ref.[18].

S7. Extended SHG polarization data from BN micro rotators: effect of substrate and bulk contributions

In the devices designed for maximizing the interface SHG contribution, the polarization patterns are determined by the D_3 symmetry of the moiré bilayer lattice and they closely follow the rotation of moiré angle. On the other hand, in devices with strong bulk SHG response, the polarization pattern reflects the reduced C_3 symmetry.

Fig. S8a shows the polarization patterns measured for Device 2 (N_{TOP}=150, N_{BOT}=138) on 285 nm SiO_2/Si substrate. Compared to polarization patterns of interface-dominated devices (see Fig. S9 and Fig. S10), bulk-dominated devices show appreciable nonzero isotropic center circles. As shown in Fig. S5c, an interference effect from the presence of the 285 nm thin film of SiO_2 on top of the Si substrate induces a significant breaking of reflection symmetry with respect to the interface plane, and thus causes strong bulk SHG contribution in this device when placed on the 285 nm SiO_2/Si substrate. With arbitrary top-bottom twist angle θ, and a broken reflection symmetry, the net symmetry has to be further reduced to only C_3. The in-plane nonvanishing elements for C_3 are $\chi^{(2)}_{xxx} = -\chi^{(2)}_{xyy} = -\chi^{(2)}_{yxy} = -\chi^{(2)}_{yyx}$, $\chi^{(2)}_{yyy} = -\chi^{(2)}_{yxx} = -\chi^{(2)}_{xxy} = -\chi^{(2)}_{xyx}$. The resulting expression for parallel-polarized SHG intensity $I_{SHG,\parallel}$ is:

$$I_{SHG,\parallel} \propto [|\chi^{(2)}_{yyy}|cos(3\varphi) + |\chi^{(2)}_{xxx}|sin(3\varphi)]^2 I^2_{pump} \quad \text{(S36)}$$

As shown by Eq. (S36), the resulting polarization pattern may not have zero nodal points. Fig. S8b shows the simulated polarization pattern from bulk and interface contributions, for a twist angle of 87.5° for the structure of Device 2 (on 285 nm SiO_2/Si substrate). The simulation is performed by the nonlinear transfer matrix method. The interface polarization shows a sixfold flower pattern with zero nodal points, while the bulk polarization has a nonzero center circle which is characteristic of the C_3 (as in Eq. (S36)). With the combination of bulk and interface effects, the total SHG polarization also shows C_3 symmetry.

In comparison, Fig. S9 shows the polarization patterns for *the same device* (Dev. 2, N_{TOP}=150, N_{BOT}=138) when it's transferred onto a bulk fused silica substrate. On a substrate such as this, with no oxide thin film below the bottom BN, the gradient of pump field is much smaller and there's significantly less SHG contribution from bulk BN (Fig. S8). In addition, Fig. S10 shows polarization patterns measured for Device 1 (N_{TOP}=7, N_{BOT}=148) on fused silica substrate, which is also optimally designed for maximizing the interface effect. The polarization patterns for both are sixfold flowers (with negligible isotropic centers) generated by the D_3 interface moiré superlattice.

S8. Fabrication of stationary devices with AB and AA' stacked interfaces

The stationary device shown in Fig. 1e in the main text, Device 0, includes both AB and AA' stacked interfaces. In order to achieve this configuration, a bulk BN crystal with uniform thickness is broken into multiple pieces during the exfoliation process, and re-stacked with 0° and 60° of relative rotation using a high-precision rotation stage in the transfer station setup [15]. Fig. S11a shows the fractured BN crystal used for assembling Device 0. Fig. S11b-h shows the pick-up sequence for the bulk BN crystal of thickness $N = 192$ layers, with regions of thickness $2N = 384$ layers that include an artificially stacked interface between the BN layers. The PPC film is first touched-down and spread over the surface of the target fractured piece, as shown in Fig. S11b. After each pick-up shown in Figs. S11c-h, the pieces of BN mounted on the surface of the PPC film above the substrate surface appear less saturated in color than the BN still mounted on the SiO_2 surface, and interfacial homostructure regions formed by overlapping BN crystals appear darker in color. At an intermediate point during assembly, the remaining target BN crystal pieces on the substrate are rotated 60° relative to the BN crystals mounted on the

PPC film, as shown in Fig. S11e. Fig. S11i shows the final twist configuration of Device 0. We observe minimal sliding of the interfaces during transfer to a fused silica substrate, and after annealing, presumably because the crystallographically aligned interfaces are at their lowest energy stacking configurations and are therefore locked in place.

This technique is adapted from those described in the supplementary information of Ref.[11] for fabrication of stationary double-aligned graphene-BN heterostructures, and can be extended to deterministically set a collection of alignment states for any broken vdW crystal with uniform layer number thickness.

S9. Mechanical relaxation near 60° twist

Atomic relaxation calculations of twisted bilayer BN near $\theta = 60^\circ$ were performed following the method presented in Ref.[39]. The function parameters of the generalized stacking fault energy were taken from Ref.[41], and the elastic coefficients of single BN layer were taken from Ref.[40]. The total energy, composed of a stacking energy term and an elastic energy term, was minimized within a continuous model to produce the local displacement fields of the relaxed system. Fig. S12a shows the stacking energy density, $E_{STACKING}$, plotted in real space over the moiré unit cell for several twist angles near $\theta = 60^\circ$. It is qualitatively apparent that as the twist angle approaches $\theta = 60^\circ$ the area of mechanically relaxed BN stacked in the energetically favorable AB or BA stacking increases.

We illustrate this onset of mechanical relaxation quantitatively in Fig. S12b, where we show a rapid increase in the percent-area taken up by AB and BA stacked BN within the moiré unit cell, and a rapid decrease in the percent-area taken up by AA stacked BN within the moiré unit cell as the twist angle decreases past 61°. The range in values of $E_{STACKING}$ assigned to the energetically degenerate AB and BA stacking is taken to be within 5 meV/nm^2 of the minimum $E_{STACKING}$ computed, and similarly the range in values of $E_{STACKING}$ assigned to AA stacking is arbitrarily taken to be within 5 meV/nm^2 of the maximum $E_{STACKING}$ computed. Any value of $E_{STACKING}$ falling outside of these ranges is labeled as *other*, a designation that dominates at large angle since the twisted BN lattices are incommensurate in this regime.

The symmetry pinning effect discussed in the main text and shown in Fig. 3f is potentially related to the rapid increase in the areal coverage of symmetry-broken AB and BA stacked BN at a twist angle near 61°. The bottom BN is much larger than the rotator, and presumably well-coupled to the fused silica substrate, mechanically. If the bottom BN can be considered microscopically stationary with respect to the lab frame, then in the presence of relaxation effects the top BN should locally twist to match the rigid bottom BN within the AB and BA domains. In this scenario the AB and BA domains would be effectively aligned to the bottom BN crystal, even though the moiré pattern itself would be at some angle θ_M. This would generate SHG inconsistent with what we predict for the non-zero global twist of the top BN rotator. This hypothesis is difficult to test without direct visualization of the buried moiré. Future experiments involving scanning probe measurements and polarization resolved SHG mapping with resolution below the scale of the moiré pattern features would resolve the microscopic symmetries and would detail the effects of mechanical relaxation. Advancements in experimental techniques combined with the modeling techniques adopted here are likely necessary to understand this symmetry pinning effect.

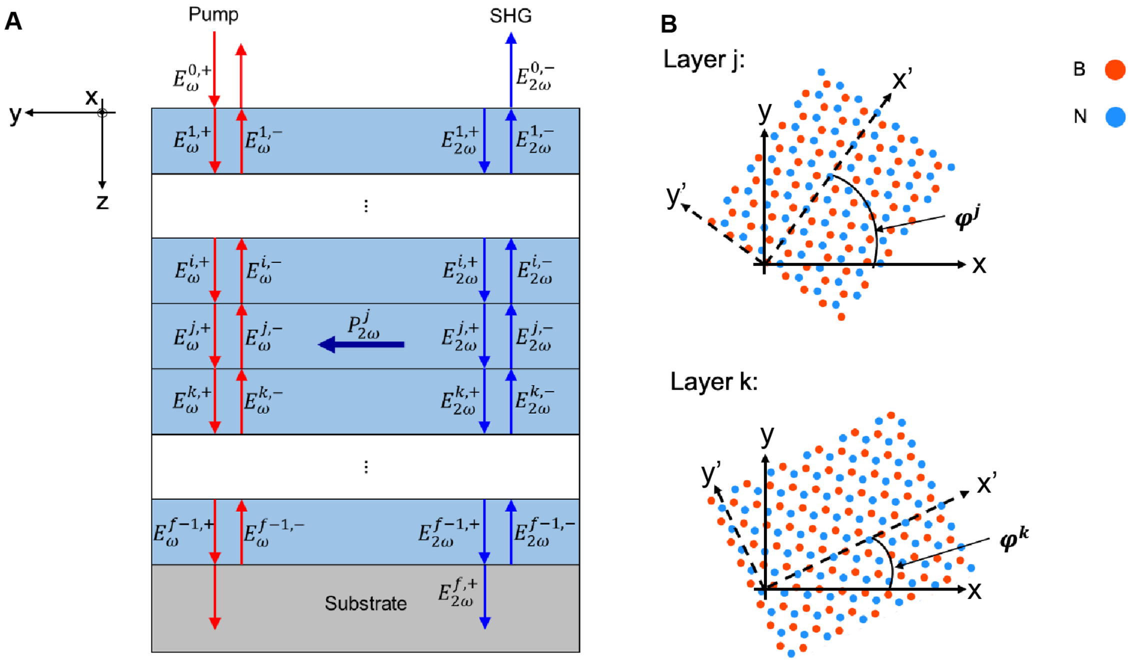

FIG. S1. **Schematic of the nonlinear transfer matrix calculation method.** (**A**) Side-view of multilayered BN on substrate. The forward- and backward-propagating pump field $E_{\omega}^{j,+}$ and $E_{\omega}^{j,-}$ generate nonlinear polarization $P_{2\omega}^{j}$ in layer j, which serves as the source for driving second harmonic field that propagates both forward ($E_{2\omega}^{j,+}$) and backward ($E_{2\omega}^{j,-}$) in the multilayers. The squared norm of reflected SHG field $E_{2\omega}^{0,-}$ corresponds to the experimentally measured quantity. The total SHG response is the coherent sum of SHG field amplitudes driven by nonlinear polarization in each layer. See text for meaning of notations and more detailed model descriptions. (**B**) Top-view of representative layer j and layer k showing the in-plane coordinate system used for calculation. The angle φ^j is defined as between the $+y$ direction in the lab frame, and the armchair direction of layer j, $+y'$ in the material frame. Arbitrary rotation angles can be implemented for each individual layers.

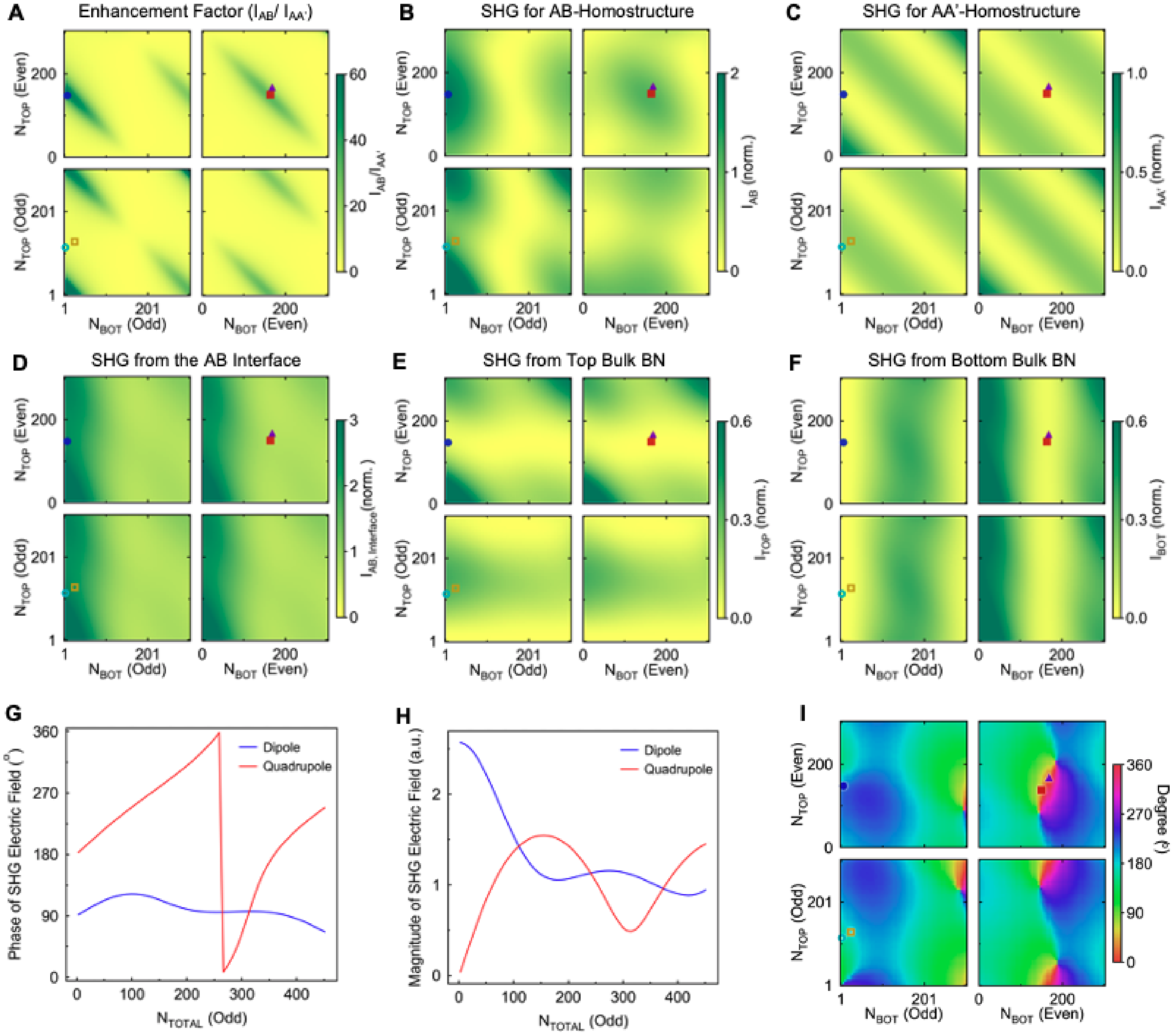

J

Dev. #		N$_{TOP}$	N$_{BOT}$	I$_{AA'}$ Exp.	I$_{AA'}$ Calc.	I$_{AB}$ Exp.	I$_{AB}$ Calc.	I$_{AB}$/I$_{AA'}$ Exp.	I$_{AB}$/I$_{AA'}$ Calc.
▲	0	168	168	0.12	0.08	0.72	0.82	6.0	10.2
●	1	148	7	0.03	0.03	1.68	1.74	56	50
■	2	150	164	0.03	0.03	1.18	1.01	40	32
□	3	129	25	0.24	0.33	0.81	0.86	3.3	2.6
○	4	115	3	0.27	0.30	1.24	1.23	4.6	4.1

FIG. S2. **Simulation results for layer-dependent SHG enhancement factor and phase shift.** (**A**), Simulation of the SHG enhancement factor $I_{AB}/I_{AA'}$ as a function of top and bottom BN layer numbers N_{TOP} and N_{BOT}, respectively, calculated by the nonlinear transfer matrix method. I_{AB} and $I_{AA'}$ represents SHG intensity for AB-homostructure and AA'-homostructure interfacial configurations, respectively. The markers tag the layer number configurations of experimentally fabricated devices with SHG results listed in the table shown by **h**. Simulation results of the SHG intensity from AB-homostructure I_{AB}, AA'-homostructure $I_{AA'}$, AB interfacial bilayer, top bulk BN, and bottom bulk BN are shown by (**B**), (**C**), (**D**), (**E**), (**F**), respectively. Data is normalized to monolayer SHG intensity of BN. (**G**), The phase of SHG electric field from dipole and quadrupole contributions, as a function of the odd total layer number N_{TOTAL}. Results for even N_{TOTAL} is not shown, since the dipole moment vanishes. (**H**), The magnitude of SHG electric field from dipole and quadrupole contributions, as a function of the odd N_{TOTAL}. (**I**), The phase shift between reflected SHG from the AB interface and the bulk, as a function of N_{TOP} and N_{BOT}. (**J**), Comparison of experimental and calculated results for all devices.

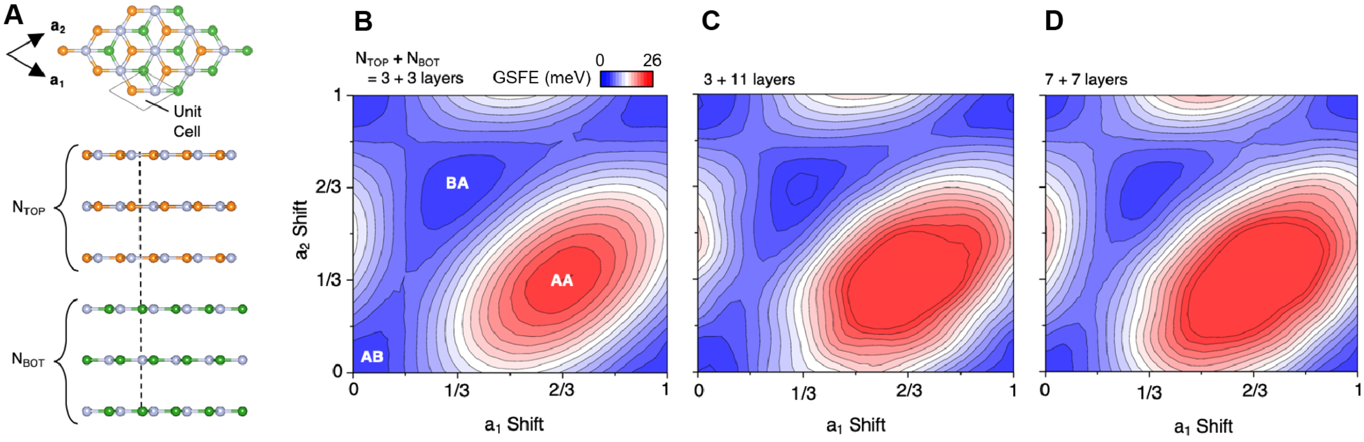

FIG. S3. **Schematic atomic structures and energy contours of BN rotators for the twisted angle of 60°.** (**A**), Top and side views of the energy minimum of BN rotator with the twisted angle of 60°. (**B**), Relative energy contour for the BN rotator with top 3 layers and bottom 3 layers. (**C**)((**D**)), Same quantity as in panel (B) for the BN rotator with top 3 (7) and bottom 11 (7) layers.

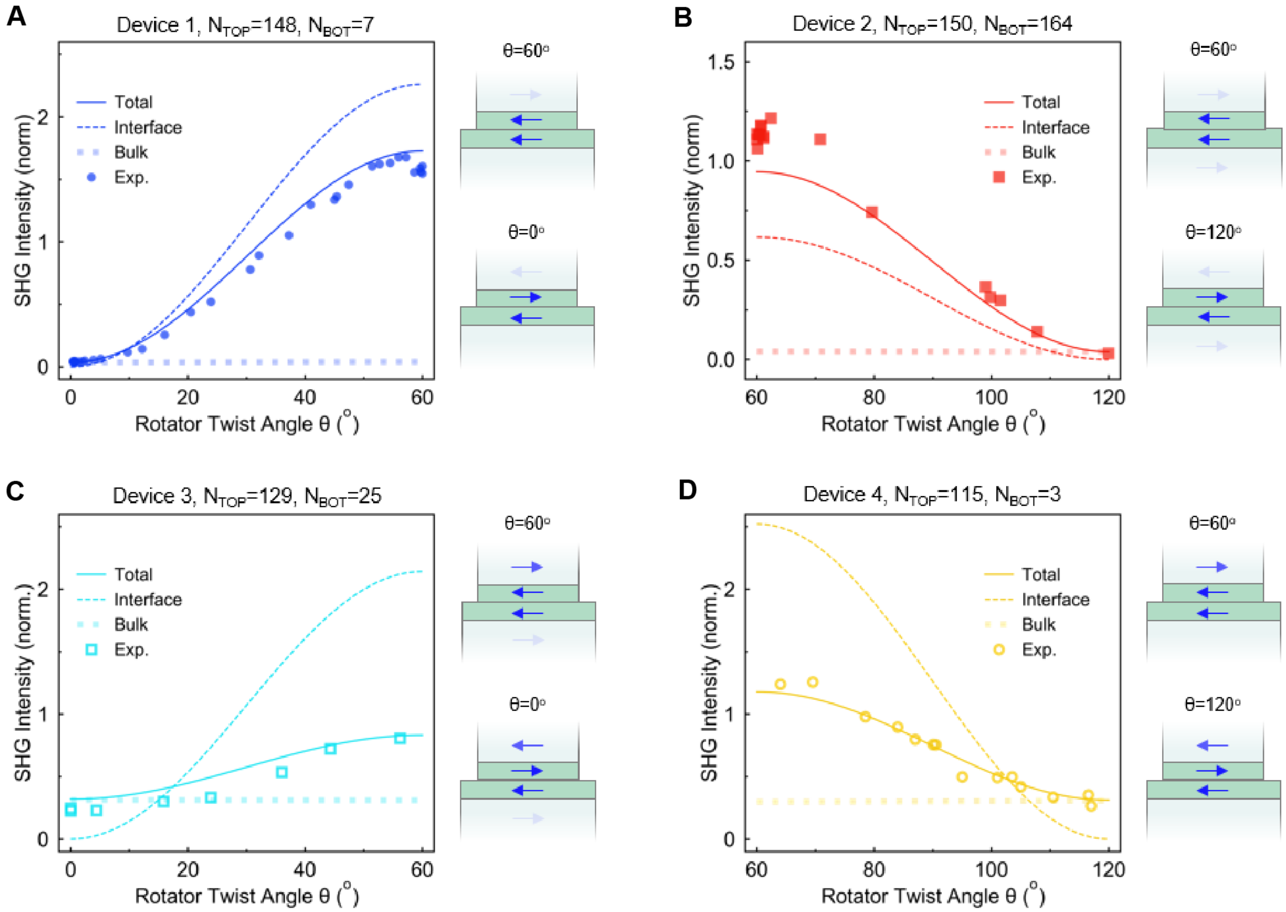

FIG. S4. **Bulk and interface SHG contributions in micro rotator devices** The results are shown for (**A**) device 1, (**B**) device 2, (**C**) device 3, and (**D**) device 4. Markers are experimental data. Solid/dashed/dotted lines are simulation results for total/interface/bulk contributions based on the nonlinear transfer matrix method. The schematics on the right side of each panel illustrate the nonlinear polarization in the interfacial bilayer (pink) and bulk parts (grey). Solid/transparent blue arrows represent high/low magnitude of nonlinear polarization.

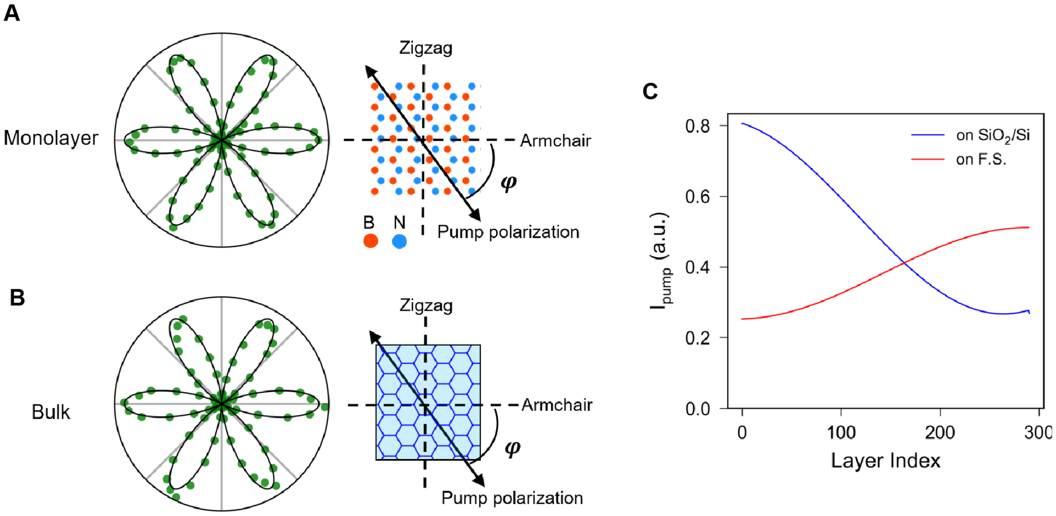

FIG. S5. **Polarization dependent SHG for (A) monolayer and (B) bulk BN.** Data are measured with the parallel polarization configuration as described in the text. For monolayer BN the sixfold pattern originates from the D_{3h} symmetry. For bulk BN, although the lattice belongs to centrosymmetric D_{3d} point group, inversion symmetry is broken by the gradient of pump field as shown in (C), resulting in a net C_{3v} symmetry whose non-vanishing $\chi^{(2)}$ elements would generate a similar sixfold polarization pattern. (**C**) The z-directional profile of pump field intensity I_{pump} calculated for a 300-layer BN on a fused silica (F.S.) and a 285-nm-SiO_2/Si substrate. The field gradient breaks reflection symmetry.

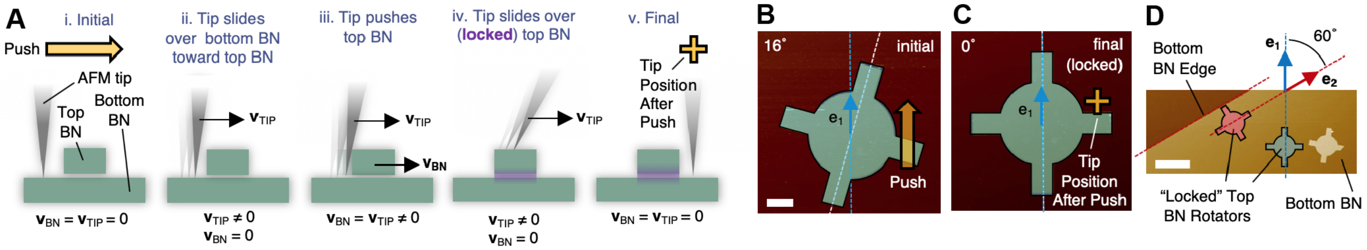

FIG. S6. **Locking behavior observed for a vdW homojunction** (**A**) Push progression through a locking state, with velocity of the top BN rotator arm, v_{BN}, and the velocity of the tip, v_{TIP}, indicated for states i-v with labels and black arrows when the velocity is not equal to zero. Yellow arrow represents the planned push, and the yellow plus-symbol represents the tip position after the push. Purple highlight added to iv-v. to indicate a locked-interface. AFM scans (**B**) before, and (**C**) after pushing the top BN crystal with an AFM tip. The rotator axis is illustrated with a white-dashed line, and the axis of a lattice unit vector (e_1, blue arrow) is illustrated with a blue-dashed line. Scale bar for (B)-(C) is 1 μm. (**D**) The locking axes of rotators are always 60° apart, as illustrated with lattice vectors e_1 (blue) and e_2 (red) parallel to the rotation axes of the two locked rotators, highlighted in blue and red. The rotator highlighted in light-blue in (D) is the same rotator shown (C) in its final state. The scale bar is 5 μm.

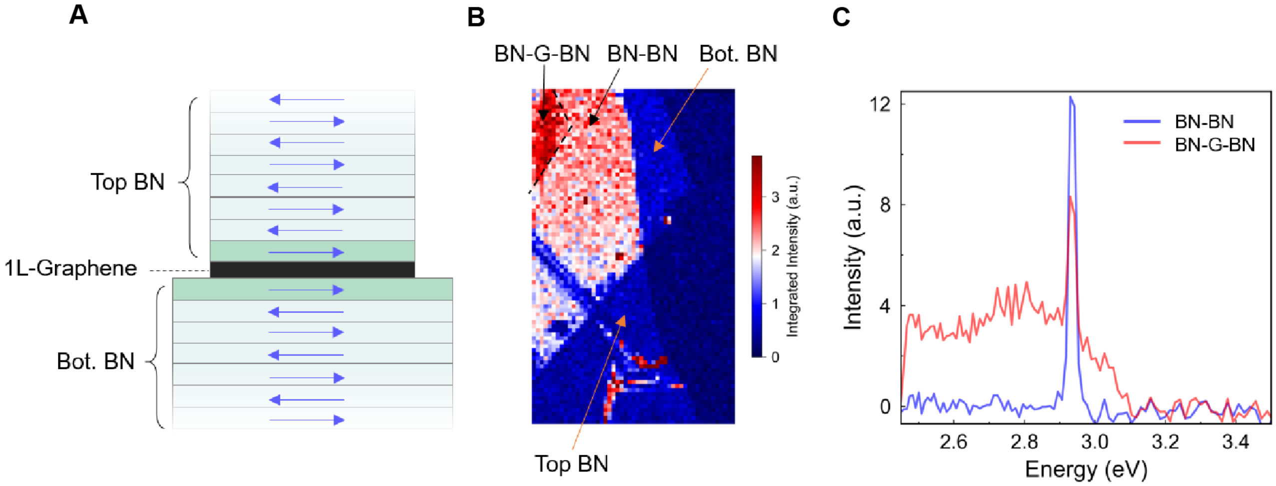

FIG. S7. **SHG from BN-graphene-BN heterostructure.** (**A**) Cross-sectional schematics of the BN-graphene-BN device. The top BN and bottom BN form AB-homostructure as in Fig. **??**A. The monolayer (1L) graphene is aligned with both top and bottom BN. (**B**) Confocal scanning image of the sample using 820 nm pulsed laser. Regions of BN-G-BN, BN-BN, and top and bottom BN crystals are labelled. (**C**) Emission spectra collected from the BN-G-BN region (red) and BN-BN region (blue). The BN-BN region shows a prominent SHG peak, while the BN-G-BN region shows much weaker SHG with a broadband fluorescence signal (likely from the graphene).

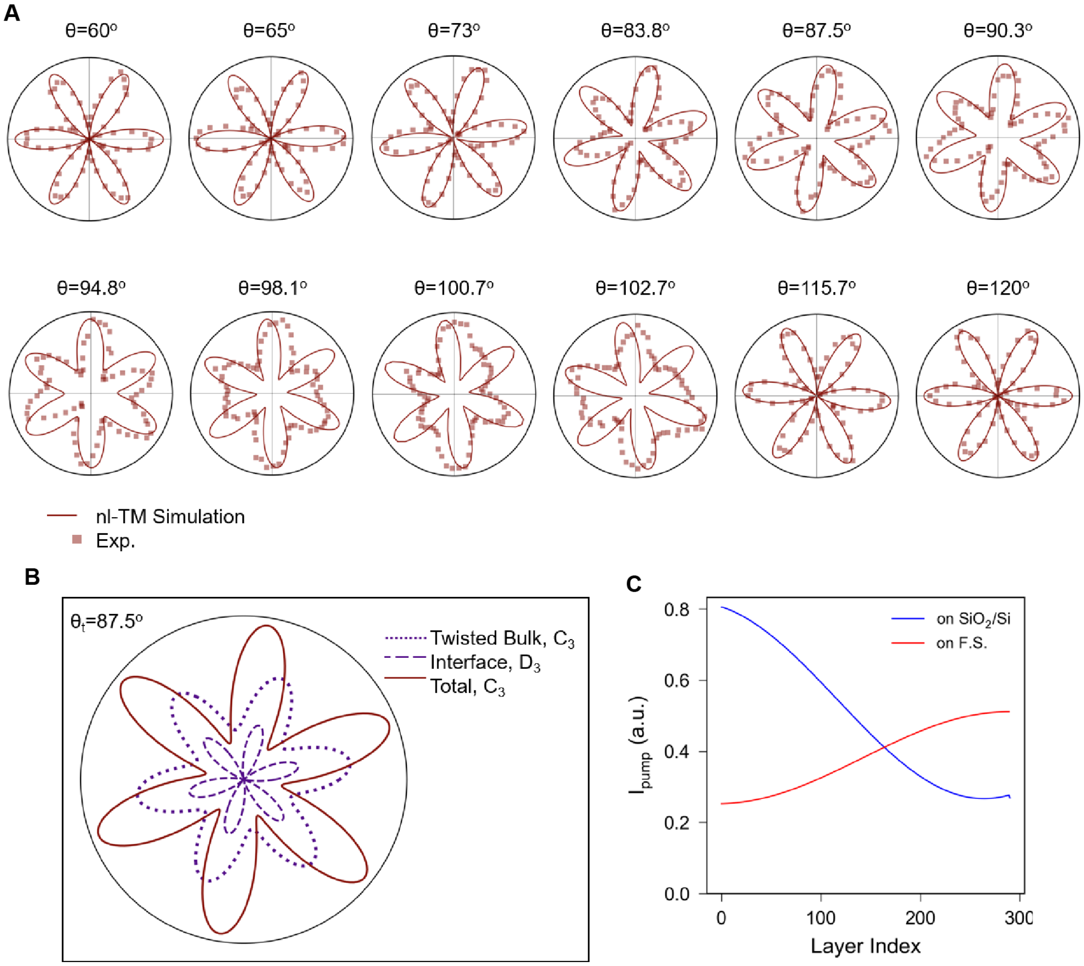

FIG. S8. **SHG polarization pattern measured for device 3 on 285 nm SiO_2/Si substrate, showing competing interface and bulk effects.** (**A**) Extended polarization data at various twist angles. Red squares are experimental data and solid lines are simulation results of this device based on the nonlinear transfer matrix method. (**B**) Simulated polarization patterns for contribution from the interface (blue dashed line), the bulk(blue dotted line), and the total device (red solid line). The interface bilayer belongs to D_3 point group, and the non-vanishig $\chi^{(2)}$ elements are $\chi^{(2)}_{xxx} = -\chi^{(2)}_{xyy} = -\chi^{(2)}_{yxy} = -\chi^{(2)}_{yyx}$. The resulting polarization pattern is a sixfold flower (without any isotropic center parts, *i.e.*, nodal points reaching zero) and maximum intensity angle aligned along the $C2(x)$ axes. The twisted bulk structure has a reduced C_3 symmetry, and has two independent sets of non-vanishig $\chi^{(2)}$ elements: $\chi^{(2)}_{xxx} = -\chi^{(2)}_{xyy} = -\chi^{(2)}_{yxy} = -\chi^{(2)}_{yyx}$, $\chi^{(2)}_{yyy} = -\chi^{(2)}_{yxx} = -\chi^{(2)}_{xxy} = -\chi^{(2)}_{xyx}$. The resultant polarization pattern will not necessarily reach zero at the nodal points and therefore shows an isotropic center pattern. (**C**) Simulated profile of pump field intensity through the BN layers. When on 285 nm SiO_2/Si substrate, interference effects result in a larger z-gradient that breaks centrosymmetry, leading to stronger bulk SHG contribution.

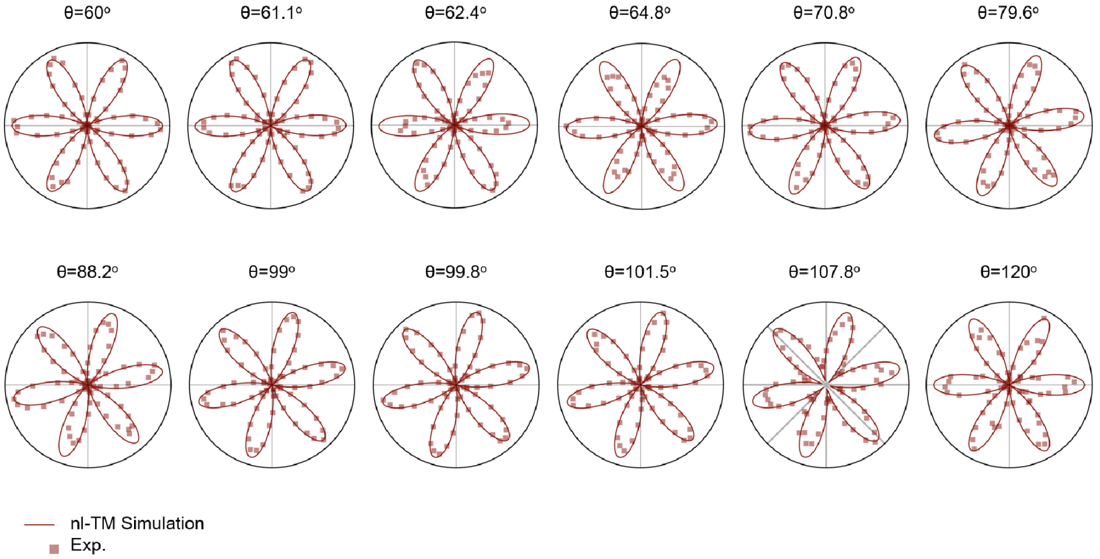

FIG. S9. **SHG polarization patterns measured for device 3 transferred onto a fused silica substrate.** Red squares are experimental data and solid lines are simulation results from the nonlinear transfer matrix calculation.

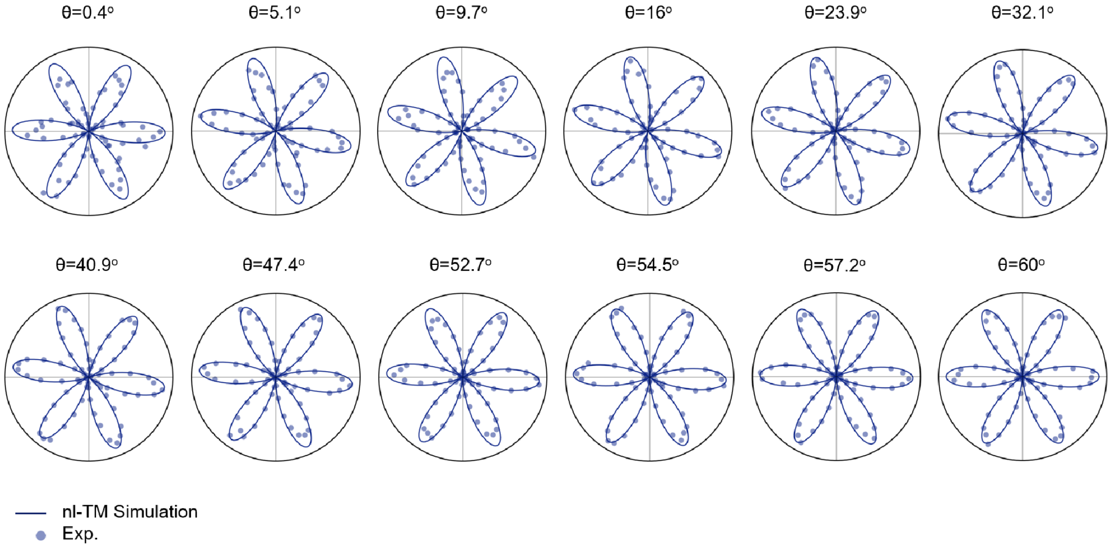

FIG. S10. **SHG polarization patterns measured for device 1 on a fused silica substrate.** Blue dots are experimental data and solid lines are simulation results from the nonlinear transfer matrix calculation.

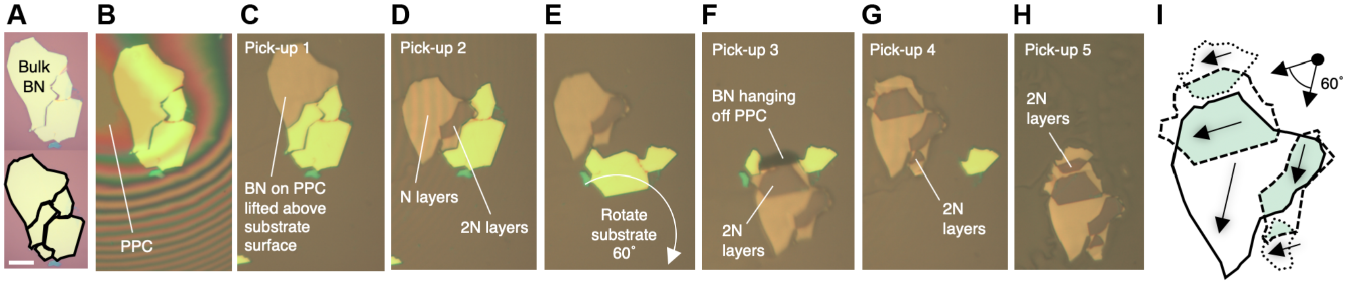

FIG. S11. **Assembly of a BN homostructure with both AB and AA' stacked interfaces.** (**A**), Bulk BN crystal on SiO_2 (top) with black outline (bottom) indicating fracture lines. Scale bar is 10 μm (**B**), Spreading of the poly-propylene carbonate (PPC) film over the BN crystal prior to pick-up 1. Touched-down region labeled as PPC, thin film interference pattern formed by the thin layer of air between the PPC and the target substrate. (**C**)-(**H**), Stack in-progress immediately following each pick-up, with an intermediate rotation of the substrate by 60° shown in (E). (**I**), Final relative twist configuration of the BN pieces for device 0 discussed in the main text, with overlap regions highlighted in light-green.

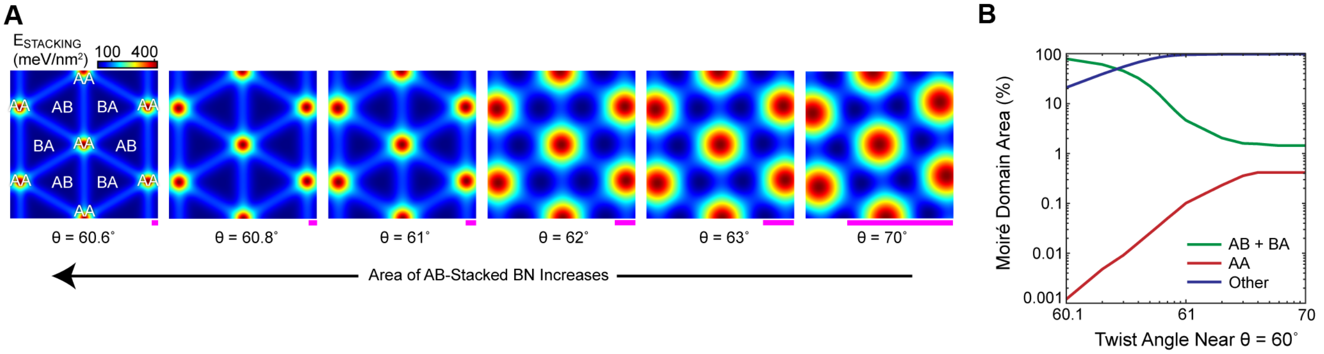

FIG. S12. **Mechanical relaxation of twisted bilayer BN near $\theta = 60°$** (**A**), Stacking fault energy density, $E_{STACKING}$, for twisted bilayer BN moiré unit cell as a function of twist angle near $\theta = 60°$. Domains identified by their corresponding stacking order are labeled on the leftmost plot. Direction of increasing AB/BA domain area indicated below. Magenta scale-bars at the lower right of each map are all 1 nm. (**B**), Moiré domain area as a function of twist angle near $\theta = 60°$. The total percent area of energetically favorable AB/BA stacking is plotted in green, energetically unfavorable AA in red, and all other stacking in blue. AB/BA (AA) stacking energy is defined as being within 5 meV/nm^2 of the minimum (maximum) $E_{STACKING}$ computed.

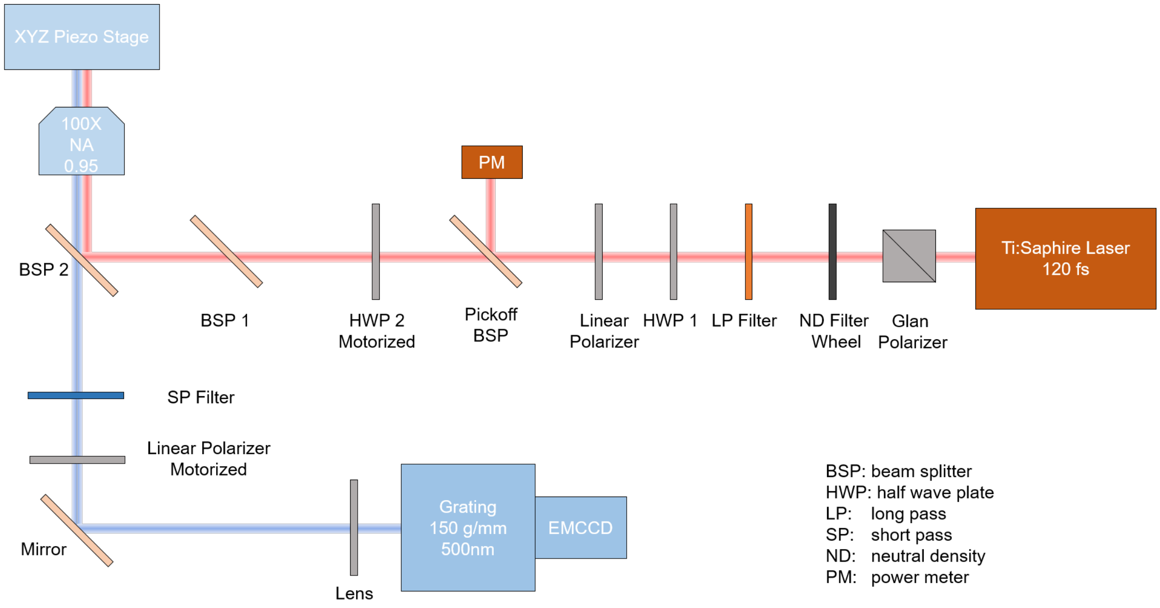

FIG. S13. **Experimental setup for SHG measurements.**

REFERENCES AND NOTES

1. Y.-R. Shen, *The Principles of Nonlinear Optics* (Wiley-Interscience, New York, 1984).

2. T. F. Heinz, Second-order nonlinear optical effects at surfaces and interfaces, in *Modern Problems in Condensed Matter Sciences* (Elsevier Science Publishers B.V., 1991), **29**, pp. 353–416.

3. R. W. Boyd, *Nonlinear Optics* (Elsevier, 2003).

4. E. Garmire, Nonlinear optics in daily life. *Opt. Express* **21**, 30532–30544 (2013).

5. M. Fiorentino, S. M. Spillane, R. G. Beausoleil, T. D. Roberts, P. Battle, M. W. Munro, Spontaneous parametric down-conversion in periodically poled KTP waveguides and bulk crystals. *Opt. Express* **15**, 7479–7488 (2007).

6. X. Zhang, Q. Cao, Z. Wang, Y. Liu, C. Qiu, L. Yang, Q. Gong, Y. Xiao, Symmetry-breaking-induced nonlinear optics at a microcavity surface. *Nat. Photonics* **13**, 21–24 (2019).

7. D. E. Chang, V. Vuletić, M. D. Lukin, Quantum nonlinear optics—Photon by photon. *Nat. Photonics* **8**, 685–694 (2014).

8. W. Cai, A. P. Vasudev, M. L. Brongersma, Electrically controlled nonlinear generation of light with plasmonics. *Science* **333**, 1720–1723 (2011).

9. K. L. Seyler, J. R. Schaibley, P. Gong, P. Rivera, A. M. Jones, S. Wu, J. Yan, D. G. Mandrus, W. Yao, X. Xu, Electrical control of second-harmonic generation in a WSe_2 monolayer transistor. *Nat. Nanotechnol.* **10**, 407–411 (2015).

10. S. Chen, K. F. Li, G. Li, K. W. Cheah, S. Zhang, Gigantic electric-field-induced second harmonic generation from an organic conjugated polymer enhanced by a band-edge effect. *Light Sci. Appl.* **8**, 17 (2019).

11. N. R. Finney, M. Yankowitz, L. Muraleetharan, K. Watanabe, T. Taniguchi, C. R. Dean, J. Hone, Tunable crystal symmetry in graphene–boron nitride heterostructures with coexisting moiré superlattices. *Nat. Nanotechnol.* **14**, 1029–1034 (2019).

12. K. Yao, E. Yanev, H.-J. Chuang, M. R. Rosenberger, X. Xu, T. Darlington, K. M. McCreary, A. T. Hanbicki, K. Watanabe, T. Taniguchi, B. T. Jonker, Zhu, D. N. Basov, Hone, P. J. Schuck, Continuous wave sum frequency generation and imaging of monolayer and heterobilayer two-dimensional semiconductors. *ACS Nano* **14**, 708–714 (2020).

13. S. Carr, D. Massatt, S. Fang, P. Cazeaux, M. Luskin, E. Kaxiras, Twistronics: Manipulating the electronic properties of two-dimensional layered structures through their twist angle. *Phys. Rev. B* **95**, 075420 (2017).

14. R. Ribeiro-Palau, C. Zhang, K. Watanabe, T. Taniguchi, J. Hone, C. R. Dean, Twistable electronics with dynamically rotatable heterostructures. *Science* **361**, 690–693 (2018).

15. K. Kim, M. Yankowitz, B. Fallahazad, S. Kang, H. C. P. Movva, S. Huang, S. Larentis, C. M. Corbet, T. Taniguchi, K. Watanabe, S. K. Banerjee, B. J. LeRoy, E. Tutuc, van der Waals heterostructures with high accuracy rotational alignment. *Nano Lett.* **16**, 1989–1995 (2016).

16. C.-J. Kim, L. Brown, M. W. Graham, R. Hovden, R. W. Havener, P. L. McEuen, D. A. Muller, J. Park, Stacking order dependent second harmonic generation and topological defects in *h*-BN bilayers. *Nano Lett.* **13**, 5660–5665 (2013).

17. W.-T. Hsu, Z.-A. Zhao, L.-J. Li, C.-H. Chen, M.-H. Chiu, P.-S. Chang, Y.-C. Chou, W.-H. Chang, Second harmonic generation from artificially stacked transition metal dichalcogenide twisted bilayers. *ACS Nano* **8**, 2951–2958 (2014).

18. E. A. Stepanov, S. V. Semin, C. R. Woods, M. Vandelli, A. V. Kimel, K. S. Novoselov, M. I. Katsnelson, Nonlinear optical study of commensurability effects in graphene-hBN heterostructures. *ACS Appl. Mater. Interfaces* **12**, 27758–27764 (2020).

19. S. Kim, J. Froch, A. Gardner, C. Li, I. Aharonovich, A. Solntsev, Second harmonic generation in multilayer hexagonal boron nitride flakes. *Opt. Lett.* **44**, 5792–5795 2019.

20. G. X. Ni, H. Wang, B.-Y. Jiang, L. X. Chen, Y. Du, Z. Y. Sun, M. D. Goldflam, A. J. Frenzel, X. M. Xie, M. M. Fogler, D. N. Basov, Soliton superlattices in twisted hexagonal boron nitride. *Nat. Commun.* **10**, 4360 (2019).

21. R. S. Pease, Crystal structure of boron nitride. *Nature* **165**, 722–723 (1950).

22. Y. Li, Y. Rao, K. F. Mak, Y. You, S. Wang, C. R. Dean, T. F. Heinz, Probing symmetry properties of few-layer MoS_2 and h-BN by optical second-harmonic generation. *Nano Lett.* **13**, 3329–3333 (2013).

23. D. S. Bethune, Optical harmonic generation and mixing in multilayer media: Analysis using optical transfer matrix techniques. *J. Opt. Soc. Am. B* **6**, 910–916 (1989).

24. T. Chari, R. Riberio-Palau, C. R. Dean, K. Shepard, Resistivity of rotated graphite–graphene contacts. *Nano Lett.* **16**, 4477–4482 (2016).

25. K. Yao, A. Yan, S. Kahn, A. Suslu, Y. Liang, E. Barnard, S. Tongay, A. Zettl, N. J. Borys, P. J. Schuck, Optically discriminating carrier-induced quasiparticle band gap and exciton energy renormalization in monolayer MoS2. *Phys. Rev. Lett.* **119**, 087401 (2017).

26. H. Ochoa, A. Asenjo-Garcia, Flat bands and chiral optical response of moiré insulators. *Phys. Rev. Lett.* **125**, 037402 (2020).

27. L. Xian, D. M. Kennes, N. Tancogne-Dejean, M. Altarelli, A. Rubio, Multiflat bands and strong correlations in twisted bilayer boron nitride: Doping-induced correlated insulator and superconductor. *Nano Lett.* **19**, 4934–4940 (2019).

28. L. Wirtz, A. Marini, A. Rubio, Excitons in boron nitride nanotubes: Dimensionality effects. *Phys. Rev. Lett.* **96**, 126104 (2006).

29. L. Wirtz, A. Rubio, Excitons in Boron Nitride Nanotubes: Dimensionality Effects, in *B-C-N Nanotubes and Related Nanostructures* (Lecture Notes in Nanoscale Science and Technology 6 Series, New York, Springer, 2009), pp. 105–148.

30. Y. R. Shen, V. Ostroverkhov, Sum-frequency vibrational spectroscopy on water interfaces: Polar orientation of water molecules at interfaces. *Chem. Rev.* **106**, 1140–1154 (2006).

31. Y. Bai, L. Zhou, J. Wang, W. Wu, L. McGilly, D. Halbertal, C. F. B. Lo, F. Liu, J. Ardelean, P. Rivera, N. R. Finney, X. Yang, D. N. Basov, W. Yao, X. Xu, J. Hone, A. Pasupathy, X. Zhu, One-dimensional moiré excitons in transition-metal dichalcogenide heterobilayers. arXiv:1912.06628 [cond-mat.mtrl-sci] (2019).

32. J. S. Lee, S. H. Choi, S. J. Yun, Y. I. Kim, S. Boandoh, J.-H. Park, B. G. Shin, H. Ko, S. H. Lee, Y.-M. Kim, Y. H. Lee, K. K. Kim, S. M. Kim, Wafer-scale single-crystal hexagonal boron nitride film via self-collimated grain formation. *Science* **362**, 817–821 (2018).

33. L. Wang, X. Xu, L. Zhang, R. Qiao, M. Wu, Z. Wang, S. Zhang, J. Liang, Z. Zhang, Z. Zhang, W. Chen, X. Xie, J. Zong, Y. Shan, Y. Guo, M. Willinger, H. Wu, Q. Li, W. Wang, P. Gao, S. Wu, Y. Zhang, Y. Jiang, D. Yu, E. Wang, X. Bai, Z.-J. Wang, F. Ding, K. Liu, Epitaxial growth of a 100-square-centimetre single-crystal hexagonal boron nitride monolayer on copper. *Nature* **570**, 91–95 (2019).

34. T.-A. Chen, C.-P. Chuu, C.-C. Tseng, C.-K. Wen, H.-S. Philip Wong, S. Pan, R. Li, T.-A. Chao, W.-C. Chueh, Y. Zhang, Q. Fu, B. I. Yakobson, W.-H. Chang, L.-J. Li, Wafer-scale single-crystal hexagonal boron nitride monolayers on Cu (111). *Nature* **579**, 219–223 (2019).

35. F. Liu, W. Wu, Y. Bai, S. H. Chae, Q. Li, J. Wang, J. Hone, X.-Y. Zhu, Disassembling 2D van der Waals crystals into macroscopic monolayers and reassembling into artificial lattices. *Science* **367**, 903–906 (2020).

36. L. Wang, I. Meric, P. Y. Huang, Q. Gao, Y. Gao, H. Tran, T. Taniguchi, K. Watanabe, L. M. Campos, D. A. Muller, J. Guo, P. Kim, J. Hone, K. L. Shepard, C. R. Dean, One-dimensional electrical contact to a two-dimensional material. *Science* **342**, 614–617 (2013).

37. A. Jain, P. Bharadwaj, S. Heeg, M. Parzefall, T. Taniguchi, K. Watanabe, L. Novotny, Minimizing residues and strain in 2D materials transferred from PDMS. *Nanotechnology* **29**, 265203 (2018).

38. A. G. F. Garcia, M. Neumann, F. Amet, J. Williams, K. Watanabe, T. Taniguchi, D. Goldhaber-Gordon, Effective cleaning of hexagonal boron nitride for graphene devices. *Nano Lett.* **12**, 4449–4454 (2012).

39. S. Carr, D. Massatt, S. B. Torrisi, P. Cazeaux, M. Luskin, E. Kaxiras, Relaxation and domain formation in incommensurate two-dimensional heterostructures. *Phys. Rev. B* **98**, 224102 (2018).

40. A. Falin, Q. Cai, E. J. G. Santos, D. Scullion, D. Qian, R. Zhang, Z. Yang, S. Huang, K. Watanabe, T. Taniguchi, M. R. Barnett, Y. Chen, R. S. Ruoff, L. H. Li, Mechanical properties of atomically thin boron nitride and the role of interlayer interactions. *Nat. Commun.* **8**, 15815 (2017).

41. S. Zhou, J. Han, S. Dai, J. Sun, D. J. Srolovitz, Van der Waals bilayer energetics: Generalized stacking-fault energy of graphene, boron nitride, and graphene/boron nitride bilayers. *Phys. Rev. B* **92**, 155438 (2015).

42. G. Kresse, J. Furthmüller, Efficient iterative schemes for *ab initio* total-energy calculations using a plane-wave basis set. *Phys. Rev. B* **54**, 11169 (1996).

43. J. P. Perdew, K. Burke, M. Ernzerhof, Generalized gradient approximation made simple. *Phys. Rev. Lett.* **77**, 3865–3868 (1996).

44. J. Klimeš, D. R. Bowler, A. Michaelides, Van der Waals density functionals applied to solids. *Phys. Rev. B* **83**, 195131 (2011).

45. S.-Y. Lee, T.-Y. Jeong, S. Jung, K.-J. Yee, Refractive index dispersion of hexagonal boron nitride in the visible and near infrared. *Phys. Status Solidi B* **256**, 1800417 (2019).